

Journal of Geophysical Research: Atmospheres**RESEARCH ARTICLE**

10.1002/2017JD027267

Key Points:

- Dust concentrations decrease with the increasing intensity of the East Asia winter monsoon (EAWM) over north China
- The feedback of changes in wind and precipitation on dust emissions contribute 67% to the variation of RF during EAWM and offset the cooling
- Wind-induced changes in dust emissions weaken the impact of EAWM on surface air temperature by 3–18% over eastern coastal China

Supporting Information:

- Supporting Information S1
- Table S1

Correspondence to:

L. M. Russell,
lmrussell@ucsd.edu

Citation:

Lou, S., L. M. Russell, Y. Yang, Y. Liu, B. Singh, and S. J. Ghan (2017), Impacts of interactive dust and its direct radiative forcing on interannual variations of temperature and precipitation in winter over East Asia, *J. Geophys. Res. Atmos.*, 122, 8761–8780, doi:10.1002/2017JD027267.

Received 8 JUN 2017

Accepted 3 AUG 2017

Accepted article online 5 AUG 2017

Published online 24 AUG 2017

Impacts of interactive dust and its direct radiative forcing on interannual variations of temperature and precipitation in winter over East Asia

Sijia Lou^{1,2} , Lynn M. Russell¹ , Yang Yang^{1,2} , Ying Liu² , Balwinder Singh² , and Steven J. Ghan² 

¹Scripps Institution of Oceanography, University of California, San Diego, La Jolla, California, USA, ²Atmospheric Science and Global Change Division, Pacific Northwest National Laboratory, Richland, Washington, USA

Abstract We used two 150 year preindustrial simulations of the Community Earth System Model, one with interactive dust and the other with prescribed dust, to quantify the impacts of changes in wind during East Asian winter monsoon (EAWM) season on dust emissions, and the resulting consequences for interannual variations of temperature and precipitation over East Asia. The simulated December–January–February dust column burden and dust optical depth are lower over northern China in the strongest EAWM years than those of the weakest years by 38.3% and 37.2%, respectively. The decrease in dust over the dust source regions and the downwind region leads to an increase in direct radiative forcing (RF) at the surface by up to 1.5 W m^{-2} . The effects of EAWM-related variations in surface winds, precipitation, and their effects on dust emissions and wet removal contribute 67% to the total dust-induced variations of direct RF at the surface and partly offset the cooling that occurs with the EAWM strengthening by heating the surface. The variations of surface air temperature induced by the changes in wind and dust emissions between the strongest and weakest EAWM years (strongest minus weakest) decrease by 0.4–0.6 K from eastern coastal China to Japan, which weakens the impact of EAWM on surface air temperature by 3–18% in these regions. The warming results from the combined effects of changes in direct RF, turbulent heat flux at the surface, and northwesterly wind anomalies that bring cold and dry air from Siberia to these regions. Over eastern coastal China, the variations of large-scale precipitation induced by the feedback of EAWM-related changes in wind on dust emissions decrease by 10–30% in winter because of the reduced changes in surface air temperature and the anomalous circulation.

1. Introduction

Dust aerosol can have adverse effects on human health and air quality, in addition to changing Earth's energy balance by scattering and absorbing radiation [Carlson and Benjamin, 1980; Sokolik and Toon, 1996; Sokolik et al., 2001]. East Asia (region 1 shown in Figure 1a) includes major dust source regions, with the largest dust concentrations originating in the Taklamakan and Gobi deserts (regions 4 and 6 shown in Figure 1a) over northern China and Mongolia, respectively [Chen et al., 1999; Merrill et al., 1989; Sun et al., 2001; Xuan and Sokolik, 2002; Zhang et al., 1996, 1997, 1998, 2003; Prijith et al., 2013]. Meanwhile, East Asia experiences significant monsoon events that are characterized by cold and dry air in winter with northwesterly winds in the lower troposphere and hot and wet air in summer with the reverse winds [Yang et al., 2014]. The effects of the East Asian Monsoon system on dust aerosols has been investigated by a number of previous measurement and modeling studies [Wu et al., 2010; Sun and Liu, 2015; Lou et al., 2016].

High dust concentrations have been observed over China and Mongolia in winter, with monthly mean concentrations of $10\text{--}100 \mu\text{g m}^{-3}$ at sites located in or near northern China and episodic dust concentrations exceeding $200 \mu\text{g m}^{-3}$ [Kanai et al., 2005; Jugder et al., 2011; Li and Zhang, 2012; Zhang et al., 2012; Wang et al., 2015]. This high dust loading can change regional climate by scattering and absorbing solar and infrared radiation (direct effect) [Miller and Tegen, 1998], heating the atmosphere and evaporating clouds (semidirect effect) [Helmert et al., 2007], and altering cloud microphysical properties (indirect effect) [Sassen, 2002]. Observation and modeling studies have shown significant dust induced radiative forcing during winter. Across China, Li et al. [2010] found that the daily mean net radiative forcing of dust is -0.3 ± 2.5 and $13 \pm 6.7 \text{ W m}^{-2}$ at the top of atmosphere (TOA) and the surface, respectively. Based on observed AOD, Angström exponents, and SSA at four desert and semidesert stations in northwestern China, Xin et al. [2016]

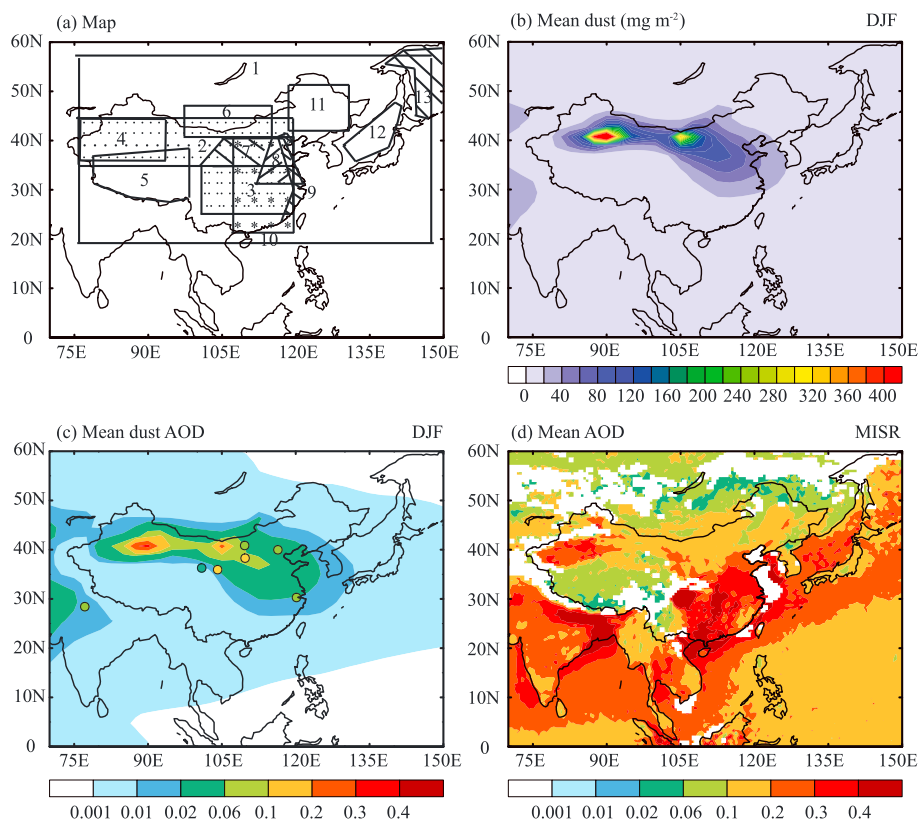


Figure 1. (a) Regional map with: (1) East Asia, (2) Northern China (dotted region), (3) Southern China (dotted region), (4) Taklamakan desert (5) Tibetan Plateau, (6) Gobi desert, (7) Loess Plateau (shaded region), (8) North China Plain (shaded region), (9) Eastern coastal China (shaded region), (10) Eastern China (star regions), (11) Northeast China, (12) Sea of Japan, and (13) Sea of Okhotsk (shaded region). (b) Simulated December-January-February (DJF) dust column burden (mg m^{-2}) averaged over 150 year IRUN simulation. (c) Simulated DJF dust optical depth (DOD) averaged over 150 year IRUN and the AERONET coarse mode AOD (dotted) with the same color bars. (d) MISR AOD for years 2000–2014 in DJF.

suggested the dust aerosol radiative forcing is in the range of 0.5 to 9 W m^{-2} at the TOA and -46 to -55 W m^{-2} at the surface in winter. Simulations also showed that the dust direct radiative forcing is from -1.5 to -15 W m^{-2} at the TOA and from -1 to -4 W m^{-2} at the surface over Taklimakan and Gobi deserts in winter [Ju and Han, 2011; Chen et al., 2014].

Previous studies have reported significant changes in surface air temperature and precipitation associated with the climatic effects of dust [Ju and Han, 2011; Yue et al., 2011; Sun et al., 2012; Zhao et al., 2015; Gu et al., 2016]. Ju and Han. [2011] reported that the wintertime surface air temperature decreased by 0.5 – 3 K over northwestern China due to the dust-induced direct radiative forcing by using the regional climate model (Regional Climate Model version 3 (RegCM3)). Yue et al. [2011] investigated the climatic effect of mineral dust aerosol using a GCM coupled with a mixed layer ocean model and suggested that the prescribed dust would change the annual mean surface air temperature by 0.15 K and -0.02 K over northern and southern China, respectively, also reducing annual mean precipitation by 0.1 mm d^{-1} over south China. Sun et al. [2012] used the Regional Climate Model version 4 (RegCM4) to show that dust aerosol cools the surface by up to 0.8 K in spring and summer in northwestern China and weakens the summer monsoon. Using the Goddard Chemistry Aerosol Radiation and Transport model, Zhao et al. [2015] reported that the dust aerosol cools the annual surface air temperature by 0.4 – 1.2 K over East Asia and decreases precipitation by up to 0.5 mm d^{-1} over northeastern China. Using the same model as Zhao et al. [2015], Gu et al. [2016] showed that dust aerosol decreases surface temperature by up to 1 K over northern China by direct radiative forcing but warms the surface by up to 0.5 K around the Tibetan Plateau area (region 5 shown in Figure 1d) by the semi-direct effect during the East Asian summer monsoon season. They also suggested that precipitation would shift northward due to the heating effect of dust over East Asia. Li et al. [2016] reviewed the interactions

between aerosol concentrations and the Asian monsoon. They reported that a weak cooling trend induced by aerosol over eastern China decreased the land-sea thermal contrast and weakened the East Asia summer monsoon circulation. In addition, dust originating from the Taklamakan desert can be transported to eastern China and the Tibetan Plateau, heating the air, altering regional atmospheric stability, and impacting the monsoon circulation.

Most of the previous studies focus on the climate effects of dust in spring and summer, but little attention has been given to the question of how dust aerosols influence interannual variations of wintertime temperatures over East Asia. A recent study [Sun and Liu, 2015] using RegCM4 suggested that dust aerosol enhances the East Asian winter monsoon (EAWM), cools surface temperatures by up to 1.5 K around the Taklamakan and Gobi deserts, and reduces precipitation by 10–30% in eastern China. However, they used prescribed SST and therefore had substantial uncertainties in their estimates of the effects of dust on climate [Miller et al., 2004; Yue et al., 2011]. No study has considered the feedback of the winds and precipitation on the dust emission, transport and removal, and how that affects the dust-climate relationship.

In this study, we use the Community Earth System Model (CESM), which includes a simulated active ocean temperature response, to quantify separately the role of EAWM-related changes in wind on dust emissions in winter and the resulting consequences for temperature and precipitation. Since the changes in winter temperatures are largely controlled by the strength of the EAWM [Hao et al., 2015] over China, we use an East Asian winter monsoon index (EAWMI) [Wang and Chen, 2014] to examine the variations in temperature between the strongest and weakest years and to identify the impact of the changes in dust emissions on those variations.

This study expands on the work of Lou et al. [2016], who used CESM to investigate the impacts of the East Asian Monsoon on dust concentrations and its direct radiative forcing in spring and suggested that interannual variations in dust emissions enhance the impact of the East Asian Monsoon on net RF over eastern China by about 40%. However, they did not investigate the impacts of changes in dust emissions on the temperature and precipitation in the region, which is the focus of this study. This study differs from Yang et al. [2017], who investigated the feedback between reduced wind-related dust emissions on further decreasing winds over eastern China, because their study was limited to the question of how the differences in dust emissions and wind speed affected modern anthropogenic aerosol concentrations over eastern China.

The description of the model and the numerical experiments is presented in section 2. Simulated variations in dust concentrations and the differences in direct radiative forcing, turbulent heat flux, surface air temperature, and precipitation between the strongest and weakest EAWM years (EAWM-related differences and strongest minus weakest) from the interactive aerosol simulation are calculated and presented in section 3. Section 3 also examines the impacts of feedback of changes in wind on dust emissions by comparing the EAWM-related differences between the interactive aerosol and the prescribed aerosol simulations. Section 4 summarizes the conclusions and implications of this study.

2. Method

2.1. Model Description

CESM includes atmosphere, ocean, land surface, and sea ice components [Hurrell et al., 2013]. Here we use CESM version 1.0.3 to simulate preindustrial conditions for 150 years, with 1.9° (latitude) by 2.5° (longitude) horizontal resolution, and 30 vertical layers from the surface to 3.6 hPa. The ocean component is the Parallel Ocean Program version 2 [Smith et al., 2010]. Properties and processes of aerosol species for mineral dust, black carbon, primary organic aerosol, secondary organic aerosol, sea salt, and sulfate are included in the aerosol module (three-mode version of Modal Aerosol Module) of CESM [Liu et al., 2012]. A trimodal log-normal distribution for Aitken (small), accumulation (medium), and coarse (large) modes are used to represent the aerosol size distribution [Liu et al., 2012], with mass and number simulated for each mode. Emission of mineral dust is treated following Zender et al. [2003] with both accumulation ($0.1\text{--}1 \mu\text{m}$) and coarse ($1\text{--}10 \mu\text{m}$) modes. Dust is assumed to be internally mixed with other aerosol components within each mode. The bulk hygroscopicity and refractive index of a single mode are calculated by volume-weighting hygroscopicities (the hygroscopicity value 0.068 is used for mineral dust) and refractive indices (obtained from Optical Properties of Aerosols and Clouds (OPAC) [Hess et al., 1998]) for each individual aerosol

component. Coating with sulfate, organic components, and water enhances solar absorption by dust aerosol through volume mixing of refractive indices. Dust optical properties are calculated as described in *Ghan and Zaveri* [2007], including extinction efficiency, absorption efficiency, and asymmetry factor. Dust is transported by the resolved winds, vertical diffusion, and cumulus mass flux, and it is removed by dry deposition, nucleation scavenging, and impaction scavenging in CAM5 [*Liu et al.*, 2012]. OPAC overestimates dust absorption and extinction compared to measurements over the Saharan desert, the Mediterranean Sea, and East Asia [*Xi and Sokolik*, 2012; *Di Biagio et al.*, 2014; *Denjean et al.*, 2016], and this apparent high bias in absorption by dust in the CESM simulations should be kept in mind.

2.2. 150 Year Simulations in Preindustrial Conditions

To identify the feedback effects of EAWM-related surface wind variability on dust emissions, we compare dust direct RF, surface air temperature, and precipitation between the strongest and weakest monsoon years for the following two simulations:

1. IRUN: The standard simulation for preindustrial conditions, with all of the greenhouse gases and anthropogenic aerosol emissions fixed at the year 1850, and using interactive dust emissions, transport, and removal.
2. PRUN: Same as the IRUN simulation but with prescribed rather than interactive dust emissions. Emissions of dust aerosol are fixed to the climatological monthly mean values of IRUN, but dust is transported and removed interactively.

Both simulations are initialized from a previous CESM simulation of 221 years with 1850 emissions, and no changes from IRUN other than prescribing dust emissions are introduced in PRUN. Both simulations allow dust as well as other components of the aerosol to affect radiative budgets and cloud properties at each time step [*Hurrell et al.*, 2013]. Comparing results from these two simulations shows the impacts of simulated interannual variations in the wind fields on dust emissions and the impacts of variations in precipitation on dust removal. Note that we compare the differences between strong and weak EAWM years in IRUN with those in PRUN simulations in this study to examine the feedback of changes in surface wind on dust emissions.

2.3. East Asia Winter Monsoon Index (EAWMI)

In order to examine the strength of the East Asian winter monsoon, a sea level pressure (SLP)-based index is used, which is defined by *Wang and Chen* [2014]. This index is determined from pressure gradients as follows:

$$\text{EAWMI} = (2 \times \text{SLP}_1 - \text{SLP}_2 - \text{SLP}_3) / 2$$

where SLP_1 , SLP_2 , and SLP_3 indicate the normalized area-averaged December-January-February mean SLP over Siberia (40° – 60° N, 70° – 120° E), the northwestern Pacific Ocean (30° – 50° N, 140° E– 170° W), and the Maritime Continent (20° S– 10° N, 110° – 160° E), respectively (the regions are shown in Figure 2c). Positive (negative) values of EAWMI represent the strong (weak) EAWM years. The interannual variations of dynamic circulation, temperature, and precipitation over East Asia in winter were well represented by EAWMI, because of the high correlation between the index and the surface air temperature anomalies, the circulation (such as Siberian high index), and the precipitation, compared to other indices [*Wang and Chen*, 2014].

In this study, we calculate the absolute difference between variables (i.e., dust, direct radiative forcing, and temperature) averaged over the strongest 10% EAWM years (15 out of 150) and those averaged over the weakest 10% EAWM years (following the definition of extreme events from Chapter 1 of the *Intergovernmental Panel on Climate Change (IPCC)* [2013], section 1.3.3) from IRUN and PRUN, respectively. The time series of EAWM index (EAWMI) are shown in Figure S1 in the supporting information; the years above and below the red lines (around ± 1.2) are chosen to be the strongest and weakest EAWM years, respectively. The difference between the strongest and weakest years in IRUN represents the magnitude of the interannual variations for winter, while the differences between IRUN and PRUN represent the effects of the interactive changes in dust emissions and removal by the simulated winds and precipitation, respectively.

3. Results and Discussion

3.1. Dust Aerosol and Meteorological Fields in Winter

Figure 1 shows the simulated climatological mean distribution of December-January-February (DJF) dust column burden and dust optical depth (DOD) at 550 nm wavelength over East Asia. High levels of dust

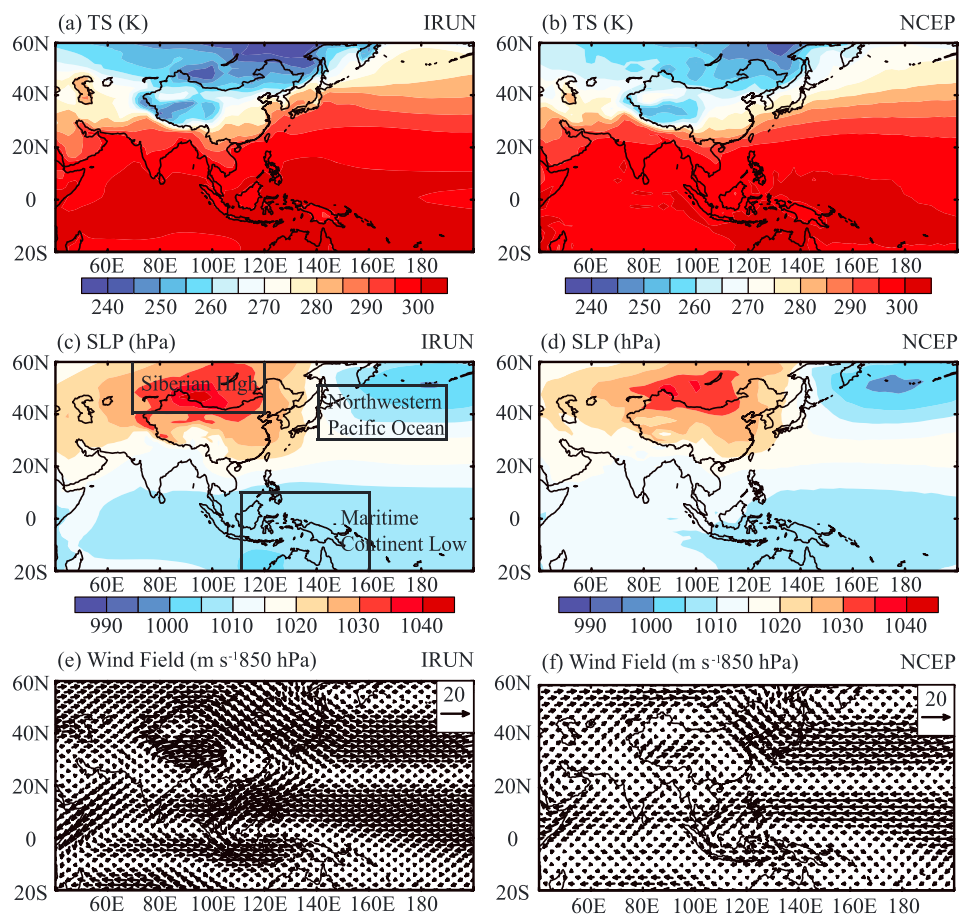


Figure 2. Spatial distribution of the climatological (a and b) surface temperature, (c and d) sea level pressure, and (e and f) wind field at 850 hPa level in DJF from IRUN simulation for 150 year (Figures 2a, 2c, and 2e) and NCEP/NCAR reanalysis data sets for years of 1948–2014 (Figures 2b, 2d, and 2f).

appear in western and central China, around the dust source regions in the Taklamakan and Gobi deserts, with a maximum column burden of 400 mg m^{-2} and a maximum DOD of 0.4. Simulated dust burden values are in the range of 5 to 100 mg m^{-2} over eastern China, with DOD values of 0.01 to 0.1. The regional means are 57.4 mg m^{-2} and 0.04 for the column burden and DOD, respectively, over northern China ($75^{\circ}\text{--}120^{\circ}\text{E}$, $35^{\circ}\text{--}45^{\circ}\text{N}$; dotted region 2 shown in Figure 1a) and 17.8 mg m^{-2} and 0.01 over southern China ($100^{\circ}\text{--}120^{\circ}\text{E}$, $22^{\circ}\text{--}35^{\circ}\text{N}$; dotted region 3 shown in Figure 1a). The high concentrations of dust over northeastern China are due to the strong northwesterlies in this region, which bring a large advected mass flux of dust aerosol from the dust source regions (the Taklamakan and Gobi deserts) [Zhao *et al.*, 2006].

The magnitude of simulated DOD is consistent with the AERONET (Aerosol Robotic Network) coarse mode AOD (details in Table S1 in the supporting information) around the dust source region and the downwind region. Moreover, since the DOD dominates the AOD in northern China close to the dust source region (e.g., regions 4 and 6 in Figure 1a), it is reasonable to compare the simulated DOD with the satellite AOD in these regions. The simulated DOD captures both the pattern and magnitude of the large AOD values in the Taklamakan and Gobi deserts compared to the average wintertime distributions of AODs retrieved from the Multi-angle Imaging SpectroRadiometer (MISR) for the years 2000 to 2012 (Figure 1d), with the largest DOD values ranging up to 0.3. The large simulated DOD pattern over Northern China also agrees with Ginoux *et al.* [2012], who retrieved seasonal DOD based on the Moderate Resolution Imaging Spectroradiometer Deep Blue Level 2 aerosol products and other data sets (including land use) for the years of 2003–2009. Over other regions, the simulated DOD values are clearly biased low because anthropogenic aerosols are present in the MISR observations but missing in the preindustrial conditions, especially over East China (star region 10 shown in Figure 1a, star region). For the surface-layer concentrations, the

simulations overestimate the annual dust loading over China by about 37% [Lou *et al.*, 2016]. The high biases of simulated preindustrial dust compared with the present-day observation are partly the result of large changes in dust source areas associated with vegetation [Tegen *et al.*, 2002; Mahowald *et al.*, 2006a, 2006b; Gu *et al.*, 2010; Xi and Sokolik, 2015]. For example, Mahowald *et al.* [2006a] reported that the dust loading in preindustrial climate is 12% higher than those in current climate, because of the changes in vegetation from changes in precipitation, temperature, and cloudiness, all of which may have been affected by anthropogenic activities since preindustrial times. Perhaps more importantly, the simulated surface wind speeds are stronger (by 6.6 and 3.2 m s⁻¹ over the Gobi and Taklamakan deserts, respectively) in preindustrial conditions than those in National Centers for Environmental Prediction (NCEP) reanalyses (which are 2.8 and 2.1 m s⁻¹, respectively) for the 2000–2012 years of the MISR observations not shown.

Although the climatological mean meteorological fields (such as SLP, temperature, and circulation) changes from the preindustrial to present-day, the spatial distribution of high or low values is likely unchanged. Simulated climatological mean SLP in IRUN shows a similar pattern to that of the National Center for Atmospheric Research (NCAR)-NCEP reanalysis mean SLP from 1948 to 2014 for DJF (Figure 2d), capturing the central positions of both the Siberian High and the Aleutian Low (Figure 2c). Northwesterlies dominate the climatological mean wind at 850 hPa in DJF for the lower troposphere over northeastern China (Figure 2e), while westerlies prevail over western China, with a strong bias of 1–2 m s⁻¹ compared to the NCAR NCEP reanalysis (Figure 2f). These SLP and wind field patterns represent fairly well the main features of the EAWM [Zhou, 2011; Wang and Chen, 2014], indicating that the model provided acceptable simulations of East Asian winter climatology. The simulated climatological surface air temperature in IRUN shows two cold centers over Siberia and the Tibetan Plateau (Figure 2a), in agreement with the NCEP reanalysis (Figure 2b). The simulated climatological mean SLP, wind fields, and surface air temperature with 1948–2014 reanalysis confirm that the model captures the structure of the EAWM system. Furthermore, the interannual variations of wind fields, temperature, and precipitation in the same simulation [Yang *et al.*, 2016a, 2016b; Lou *et al.*, 2016] provide an acceptable simulation of the interannual variations of EAWM strength.

3.2. Interannual Variations of Dust Concentration and Its Direct Radiative Forcing Due to the Wind-Induced Changes in Dust Emissions During Winter

In order to investigate the variations of dust during winter, the absolute differences between the dust column burden and DOD averaged over the 10% strongest EAWM years and those averaged over the 10% weakest EAWM years from the IRUN simulation are calculated and shown in Figures 3a and 3b, respectively, following the definition of the highest 10% as the “extreme events” [IPCC, 2013]. The dust column burden and DOD in the strongest EAWM years are lower than the weakest EAWM years (by 38% on average) over northern China, with the largest reductions over the Taklamakan and Gobi deserts in the ranges of 80 to 140 mg m⁻² and 0.04 to 0.12, respectively. The decrease in dust and DOD correspond to the composite differences of the 850 hPa winds between the strongest and weakest EAWM years (Figure 8e). Northeasterly anomalies are shown over northeastern China (region 11 shown in Figure 1a) and the Gobi desert while easterly anomalies over the Taklamakan desert in strong EAWM years, consistent with the changes in wind identified by Wang and Chen [2014]. Therefore, the reductions in dust burdens result from the lower dust emissions associated with easterly anomalies over the Taklamakan desert and from lower transport fluxes through the Gobi desert to eastern China due to the changes in wind direction in these regions (dust emissions in strongest and weakest EAWM years are shown in Figure S2). The differences in TOMS AI (Total Ozone Mapping Spectrometer Aerosol Index) in strong EAWM years compared to those in weak EAWM years (based on the NCEP reanalysis, time series of EAWMI is shown in Figure S1) are shown in Figure 3c. Note that the TOMS AI is an indicator for all evaluated absorbing aerosols, including biomass burning particles in addition to dust. Therefore, we chose the period from 1978 to 1993 to compare to the preindustrial simulations, since the anthropogenic emissions in China were lower than after 2000. The TOMS AI also showed smaller values in strong EAWM years than those in weak EAWM years in northern China, consistent with the simulated DOD shown in Figure 3b.

To determine the radiative forcing associated with these changes in dust concentrations and distributions, the EAWM dust direct radiative forcing is calculated as the difference in the direct radiative forcing of all aerosols between the 10% strongest and 10% weakest EAWM years (strongest minus weakest). The direct radiative forcing of all aerosols is diagnosed for each simulation from the difference of the radiative flux with and

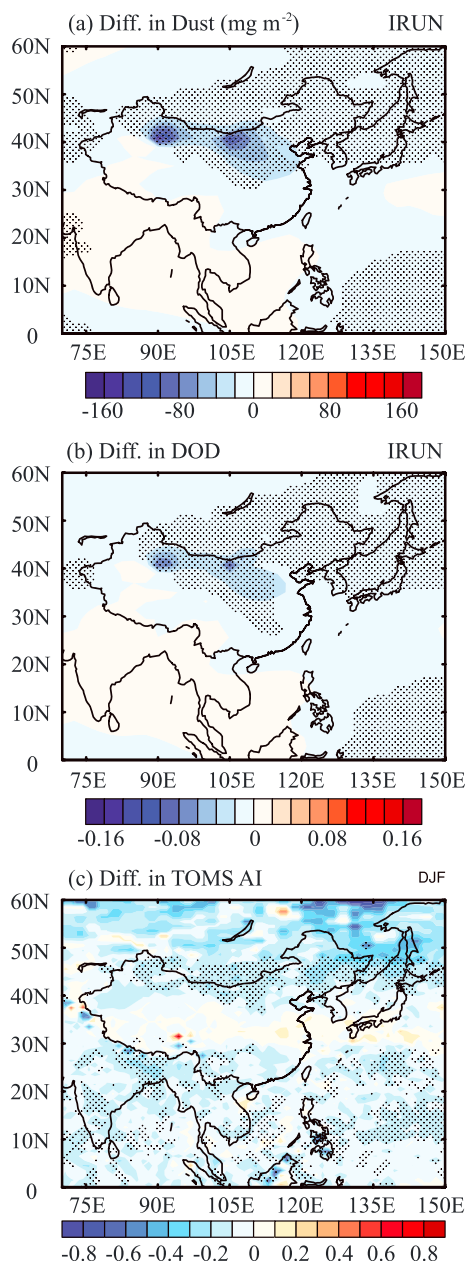


Figure 3. Horizontal distributions of absolute differences in (a) dust column burden (mg m^{-2}) and (b) dust optical depth (DOD) between the strongest and weakest EAWM years (strongest-weakest) in DJF calculated from IRUN. (c) The differences in TOMS AI between EAWM years calculated from NCEP/NCAR reanalysis data sets for years of 1978–1993. The dotted areas indicate statistical significance with 95% ($P < 0.05$) from a two-tailed Student's t test.

to the strongest EAWM years, the long-wave radiative forcing (LWRF) is smaller in the weakest EAWM years over a large fraction of China in the IRUN simulation (Figures 4c and 4d), due to the decrease in dust column burden and DOD (Figures 3a and 3b), with the maximum LWRF values of -1.5 and -2 W m^{-2} at the surface over the Gobi and Taklamakan deserts, respectively. The dust-induced surface total radiation change (SW + LW) between the strongest and weakest EAWM years (strongest minus weakest) over East Asia was positive with a magnitude of $+1.5 \text{ W m}^{-2}$ over the North China Plain, and the Gobi and Taklamakan deserts (Figure 4e). The radiation change at the TOA had a similar pattern with smaller magnitude changes than those at the surface. The simulated dust-induced changes in surface radiation in this study agree with the

without the scattering and absorption of solar radiation by all of the aerosols [Ghan, 2013]. The climatological mean direct radiative forcing induced by dust are shown in Figure S3. Figure 4 shows the simulated differences in all-sky dust direct radiative forcing for the solar flux, long-wave flux, and the net flux at the surface (Figures 4a, 4c, and 4e) and the top of atmosphere (TOA) (Figures 4b, 4d, and 4f) between the 15 (i.e., 10%) strongest and the 15 weakest EAWM years from the 150 year IRUN simulation. The simulated differences in shortwave radiative forcing (SWRF) are mostly positive over China, with maximum values of 2, 3, and 3.5 W m^{-2} at the surface and of 1, 0.5, and 1 W m^{-2} at TOA over the North China Plain (shaded region 8 shown in Figure 1d), the Gobi desert, and the Taklamakan desert, respectively (Figures 4a and 4b), resulting from the decreased dust concentrations (DOD) of up to 60 mg m^{-2} (0.04), 100 mg m^{-2} (0.08), and 140 mg m^{-2} (0.08) for these same regions (Figures 3a and 3b). Our results are consistent with Sun and Liu [2015], who reported that the dust-induced clear-sky SWRF decreased by $6\text{--}16 \text{ W m}^{-2}$ at the surface and $0.5\text{--}4 \text{ W m}^{-2}$ at TOA due to DOD values in the range of 0.2 to 0.3 over northwestern China in winter for the years of 2000 to 2009 using RegCM4. There is also a strong positive SWRF over the Philippine Sea between the strongest and weakest EAWM years (strongest minus weakest), both at the surface and TOA, mainly due to the decrease in sea-salt aerosol associated with the changes in wind speed [Yang et al., 2016c]. Relative

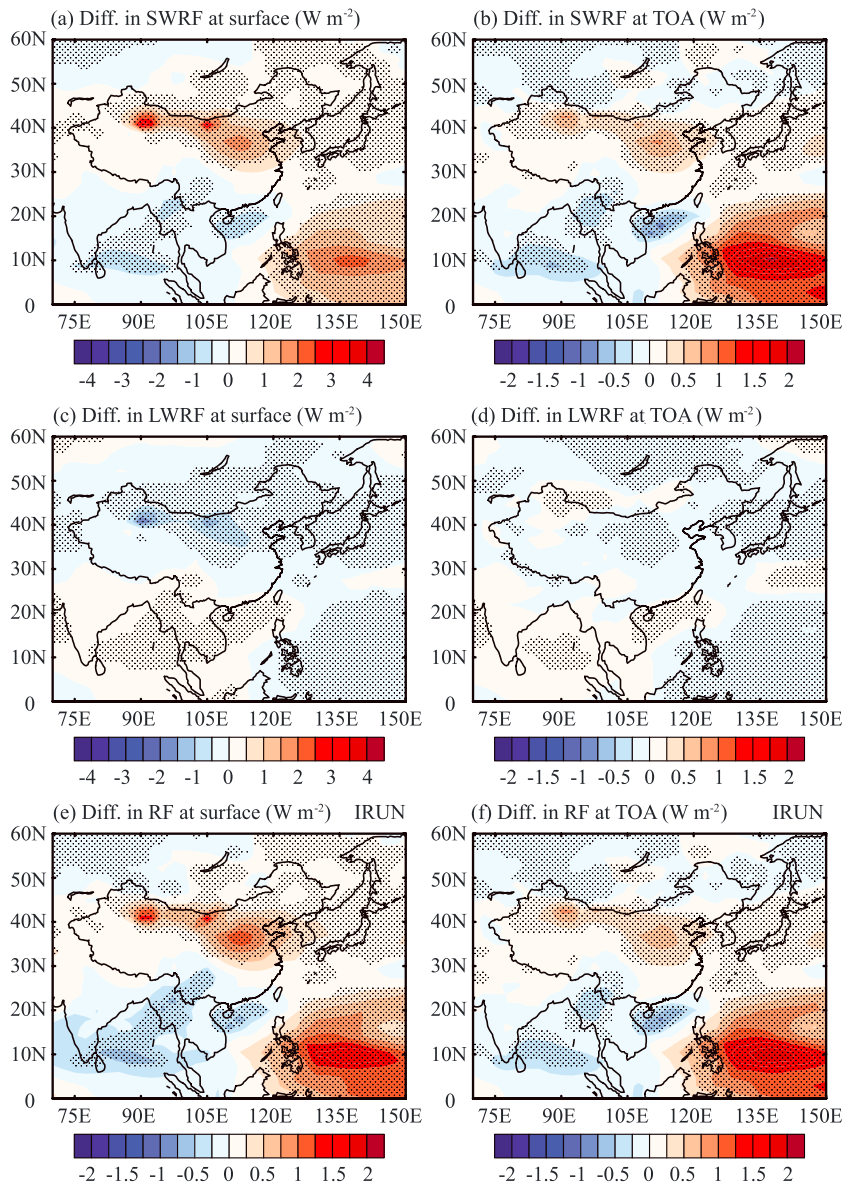


Figure 4. The direct radiative forcing differences in (a and b) solar flux, (c and d) long-wave flux, and (e and f) total flux by dust between the strongest and weakest EAWM years (strongest–weakest) in the IRUN. Figures 4a, 4c, and 4e show changes at the surface, and Figures 4b, 4d, and 4f show changes at the top of the atmosphere (TOA). The dotted areas indicate statistical significance with $95\% (P \text{ value} < 0.05)$ from a two-tailed Student's t test. Positive (negative) value refer to net downward (upward) flux.

simulation of *Chen et al. [2014]*, who suggested that the regional mean dust direct radiative forcings at the surface in DJF are -2 , -2.5 , and -3 W m^{-2} over the North China Plain, the Gobi and the Taklamakan deserts, respectively, with the dust loading (DOD) values in the range of $70\text{--}140 \text{ mg m}^{-2}$ ($0.06\text{--}0.12$), $120\text{--}300 \text{ mg m}^{-2}$ ($0.12\text{--}0.22$), and $180\text{--}300 \text{ mg m}^{-2}$ ($0.1\text{--}0.25$) for DJF, based on simulations from the Weather Research and Forecasting model with Chemistry for years 2007 to 2011. Given the decrease in surface air temperatures in the strongest EAWM years in northern China, the radiative flux changes imply that the dust aerosol partially offsets the EAWM winter cooling effect by its direct forcing.

The differences in SWRF, LWRF, and net RF at the surface and TOA induced by dust aerosol in PRUN between the strongest and weakest EAWM years show similar patterns as IRUN but with smaller magnitudes (not shown). To examine the impacts of feedback of the changes in surface winds on dust emissions, we compare the variations of dust concentrations and radiative forcing in the interactive IRUN simulation to those in the

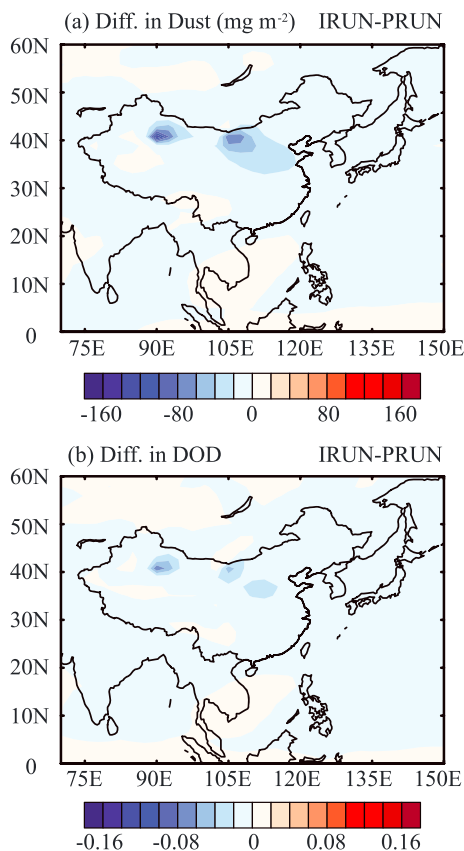


Figure 5. Horizontal distributions of differences in EAWM (a) dust column burden and (b) dust optical depth (DOD) calculated between IRUN and PRUN simulations. The EAWM dust burden and DOD are the differences of those variables between the strongest and weakest EAWM years (strongest-weakest).

2.5 W m⁻² over the Taklamakan desert, respectively, at the surface and of up to 0.75 and 0.5 W m⁻² at the TOA (Figures 6a and 6b). These results indicate that the effects of changes in surface winds on dust emissions over East Asia enhance the differences in dust concentrations and its SWRF between the strongest and weakest EAWM years by about 70% over China. The difference in LWRF between the strongest and weakest EAWM years for the prescribed dust emissions (PRUN) simulation is quite small at the surface but has small positive values over the southern part of the Taklamakan desert because of the small anomalous easterlies that lead to less transport of dust from this region and concentrate the dust near the sources (not shown). The largest changes in LWRF of up to -1 and -1.5 W m⁻² at the surface over the Gobi and Taklamakan deserts (Figure 6c), respectively, and of no more than -0.25 and $+0.25$ W m⁻² at the TOA in IRUN compared to those in PRUN indicate that the wind-driven decreases in dust emissions in strong EAWM years also enhance the LWRF during strong EAWM years.

The decrease in dust column burden between the strongest and weakest EAWM years (strongest minus weakest) leads to higher dust direct radiative forcing in IRUN compared to PRUN, with maximum values of up to 1 W m⁻² at the surface and 0.75 W m⁻² at the TOA over eastern central China (Figures 6e and 6f). Over western China, RF is also positive at the surface by up to 1 W m⁻², but it has small positive or negative values at the TOA depending on the albedo [Liao and Seinfeld, 1998]. Since the changes in dust could offset the EAWM cooling by heating the surface (as discussed above), the wind-induced changes in local dust emissions contribute about 67% to heating during EAWM from the dust direct radiative forcing compared to the variations of net RF in IRUN relative to those in PRUN. However, as noted above, the dust in the simulations is likely excessively absorbing in the shortwave, so the heating is likely overestimated.

prescribed dust PRUN simulation. However, it should be noted that there are too few samples (only four values, the mean values of the strongest years, and weakest years for both IRUN and PRUN simulations) for a student's test to calculate the significance. The composite differences in EAWM dust and direct RF at the surface (strongest minus weakest) between IRUN and PRUN (shown in Figures 5 and 6, respectively) show the contribution of the wind-induced changes on dust emissions. Larger reductions in EAWM (strongest minus weakest) dust column burden and DOD are found in IRUN compared to PRUN over large fractions of China (Figures 5a and 5b), with the largest values of -60 mg m⁻² and -0.06 over the Taklamakan and Gobi deserts and of -40 mg m⁻² and -0.04 over downwind regions (such as the North China Plain). Therefore, the differences in SWRF between the strongest and weakest EAWM years are larger over almost all of China in IRUN than those in PRUN, with differences of up to 1.5 W m⁻² both over the Loess Plateau (shaded region 7 shown in Figure 1a) and the North China Plain and

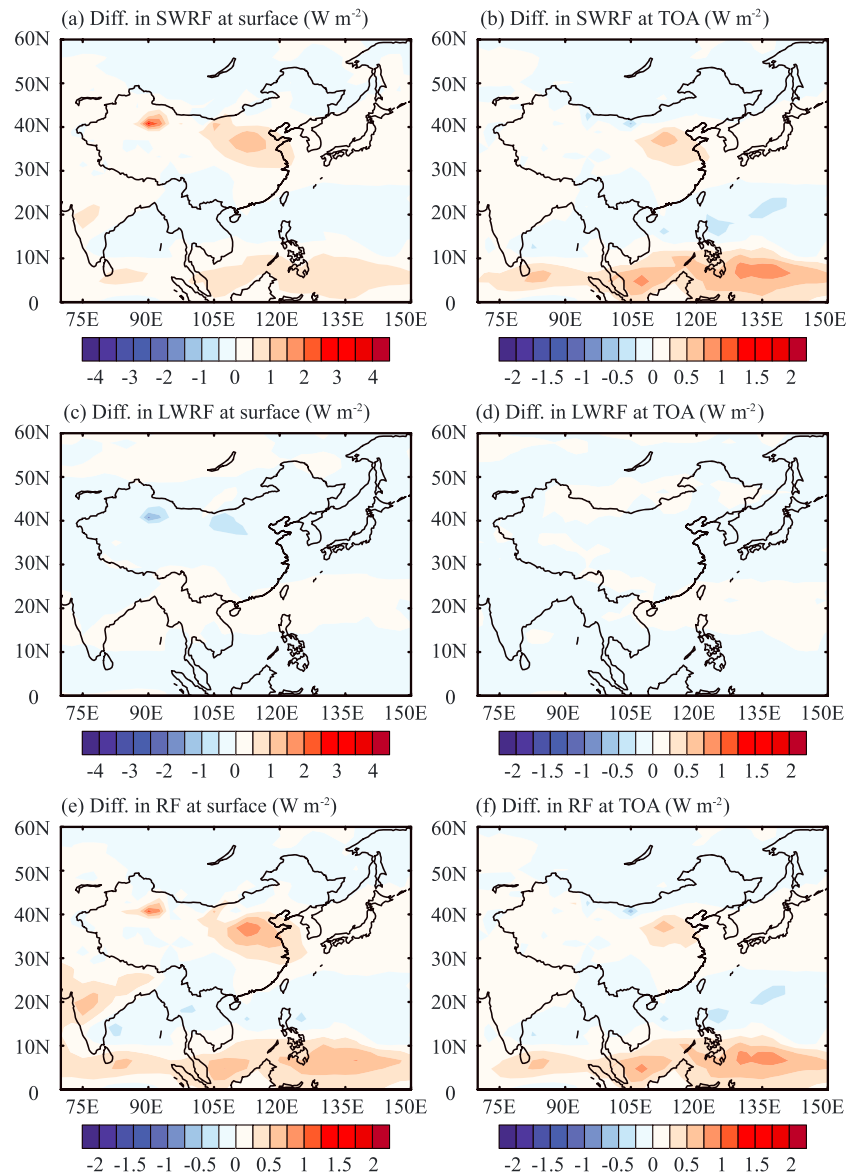


Figure 6. The same as Figure 4 but with the differences in EAWM direct radiative forcing calculated between IRUN and PRUN simulations.

3.3. Interannual Variations of Turbulent Heat Flux at the Surface Due to the Wind-Induced Changes in Dust Emissions During Winter

In order to investigate the variations of energy budget at the surface, the absolute differences between the sensible heat flux (SHFLX), latent heat flux (LHFLX), and the total turbulent heat flux (THFLX) at the surface over the 10% strongest EAWM years and those averaged over the 10% weakest EAWM years from the IRUN simulation are calculated and shown in Figures 7a, 7c, and 7e (the climatological mean SHFLX, LHFLX, and THFLX are shown in Figure S4). The EAWM-related SHFLX are found to increase by 3–6 W m^{-2} over East China and Northeast China (Figure 7a) and indicate that the larger heat energy is transferred from the surface to the atmosphere by conduction and convection in the strongest EAWM years than those in weakest EAWM years in these regions. The simulated differences in THFLX (SHFLX + LHFLX; Figure 7e) are found to be positive over central China and eastern coastal China between strongest and weakest EAWM years (strongest minus weakest) due to the variations of SHFLX, agree with previous studies who also reported more heat energy transferred to the atmosphere in strong EAWM years [Shiota *et al.*, 2011; Kim

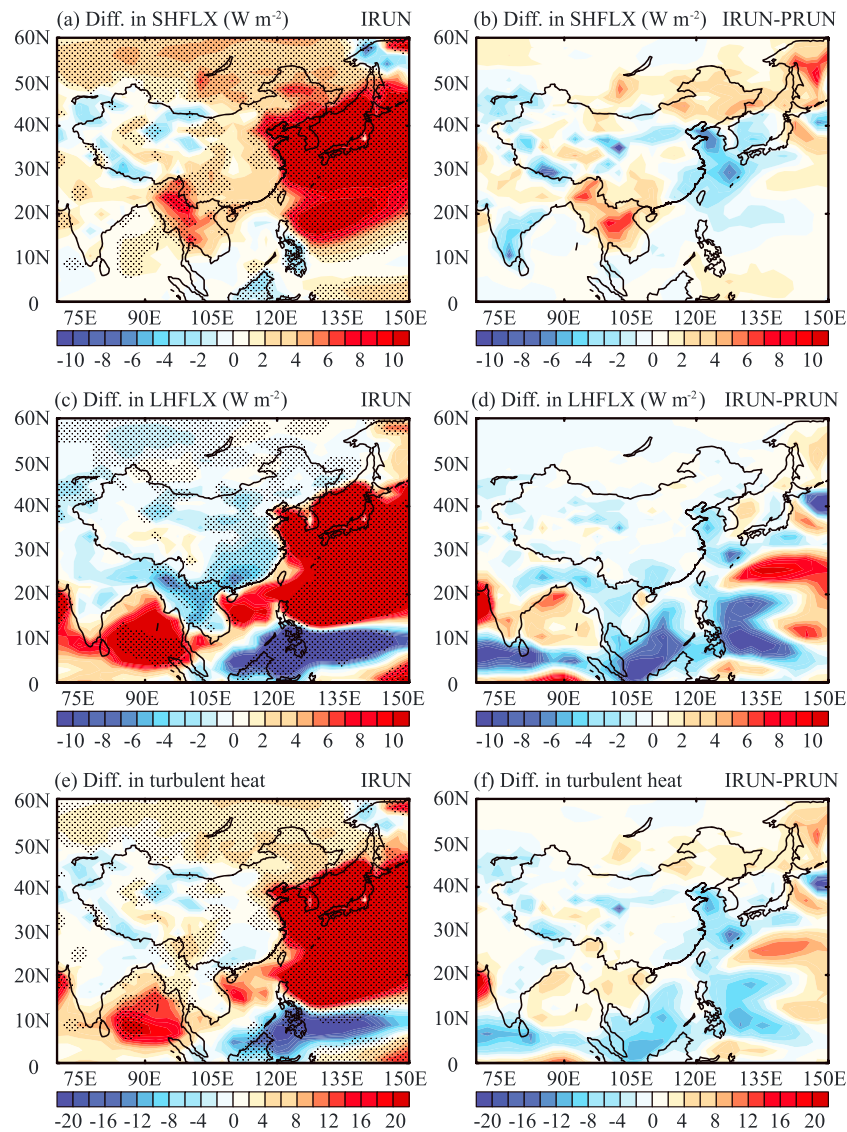


Figure 7. The differences between strongest and weakest EAWM years (strongest-weakest) from IRUN and the differences between IRUN and PRUN in (a and b) sensible heat flux, (c and d) latent heat flux, and (e and f) total turbulent heat flux at the surface. The dotted areas indicate statistical significance with 95% (P value < 0.05) from a two-tailed Student's t test.

et al., 2013] and cooling the surface. Over south China, the less THFLX are found in the strongest EAWM years than those in the weakest EAWM years by up to 4 W m^{-2} due to the negative variations in LHFLX (Figure 7c), which illustrates the less heat energy transferred to the atmosphere with the enhanced strength of EAWM in this region.

To examine the impacts of feedback of the changes in surface winds on dust emissions, we also compare the variations of heat energy fluxes in the interactive IRUN simulation to those in the prescribed dust PRUN simulation. The composite differences in SHFLX, LHFLX, and THFLX at the surface (strongest minus weakest) between IRUN and PRUN (Figures 7b, 7d, and 7f) show the contribution of the wind-induced changes on dust emissions. Relative to PRUN, the EAWM-related variations in THFLX are found to be negative over eastern coastal China and the East China Sea in the strongest EAWM years than those in weakest EAWM years (Figure 7f); indicate the smaller variations of surface heat energy in IRUN by up to 4 and 12 W m^{-2} , respectively; and reduces the EAWM-related cooling at the surface in these regions. The variations in surface heat energy are found to have larger negative values in IRUN than those in PRUN around the Tibetan Plateau

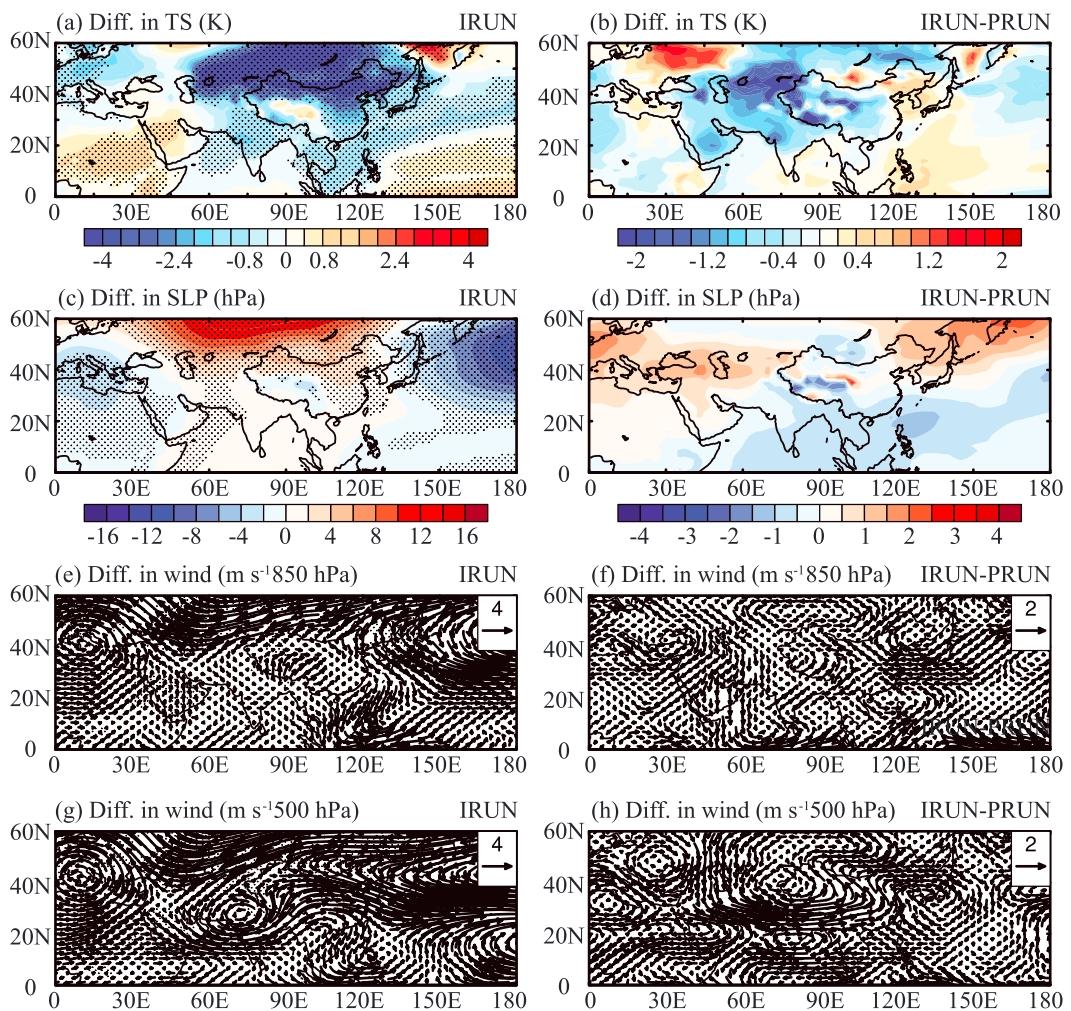


Figure 8. The differences between strongest and weakest EAWM years (strongest-weakest) from IRUN and the differences between IRUN and PRUN in (a and b) surface air temperature (K), (c and d) sea level pressure (hPa), (e and f) horizontal winds at 850 hPa, and (g and h) horizontal winds at 500 hPa, respectively. The dotted areas indicate statistical significance with 95% (P value < 0.05) from a two-tailed Student's t test.

by 4–8 W m^{-2} . The magnitude of variations in surface heat energy are much larger than the dust-induced differences in net RF at the surface between IRUN and PRUN (Figure 6e).

3.4. Interannual Variations of Surface Air Temperature and Precipitation Due to the Wind-Induced Changes in Dust Emissions During Winter

The simulated differences in surface air temperature between the strongest and weakest EAWM years are shown in Figure 8a. In strong EAWM years, significant cooling is found from over central Siberia and extending to a large fraction of East Asia and the northwestern Pacific Ocean. Comparing the difference in surface air temperatures in the IRUN and PRUN simulations shows the impacts of simulated wind fields on dust emissions and the resulting variations of temperature. The differences in surface air temperature between the strongest and weakest EAWM years (10% strongest minus 10% weakest) are calculated for both the interactive and prescribed dust emission simulations to quantify the interannual variations. The EAWM-related cooling effects are smaller in IRUN than those in PRUN and show positive anomalies over eastern coastal China to the Sea of Japan (Figure 8b, region 12 shown in Figure 1a) by up to 0.4 K and over northeastern China by 0.6 K, partly resulting from the strong positive dust-induced radiation change at the surface (Figure 6e), and the EAWM-related smaller energy heat at the surface (Figure 7f).

To investigate the variations in surface air temperature, the differences in surface-layer solar heating rate (QRS), longwave heating rate (QRL), temperature tendency due to moist process (DTCOND), and temperature vertical diffusion (DTV) are calculated between the strongest and weakest EAWM years in IRUN (strongest minus weakest) and are shown in Figure 9 (the climatological mean QRS, QRL, DTCOND, and DTV are shown in Figure S5). Although the QRS show the largest negative values over dust source regions (such as the Taklamakan and Gobi deserts; Figure 9a), the total heating rate at the surface-layer shows positive values over a large fraction of China (Figure 9i) and indicates the small contribution from dust direct radiative forcing to the variations of surface air temperature. Over eastern coastal China and the East China Sea, the smaller EAWM-related changes in surface-layer heating rate are found in IRUN than that in PRUN (Figure 9j) due to the weaker variations of DTCOND (Figure 9h) and the stronger variations of QRS (Figure 9b). Over western and central China, the variations of DT between IRUN and PRUN are dominated by the variation of DTV (Figures 9f and 9j). Comparing the difference in surface-layer heating rate in IRUN and PRUN, the magnitude of variations in DTCOND and DTV are much larger than QRS, suggested that the dynamic changes due to the feedback of wind field on dust emissions dominated the variations in surface air temperature, not the dust-induced RF.

Therefore, the major reason for the smaller variations in surface air temperature in IRUN than those in PRUN is the changes in SLP. The differences in SLP are lower over Mongolia and higher between northeastern China and the Sea of Okhotsk (shaded region 13 shown in Figure 1a) in IRUN compared to PRUN (Figure 8d) between the 15 (10%) strongest and weakest EAWM years (strongest minus weakest). The differences in EAWM-related SLP between IRUN and PRUN show weak variations of northwesterly wind in the lower troposphere over northeastern China and eastern coastal China and show easterly and southerly anomalies that result from the feedback of changes in wind on dust emissions (Figure 8f). Considering the larger cold advection in strongest EAWM years than those in weakest EAWM years (Figures 8a and 8e), the smaller changes in thermal advection associated with the weaker variations of northwesterlies over northeastern China and eastern coastal China lead to smaller variations of surface air temperature in IRUN than those in PRUN in these regions and show positive anomalies in Figure 8b. Compared to the EAWM-related cooling effect of 1 to 3.5 K in the interactive simulations (strongest minus weakest), the positive anomalies in surface air temperature associated with the feedback from the changes in wind on dust emissions (Figure 8b) indicate that the interannual variations in dust emissions weaken the impact of EAWM on surface air temperature by 3–18% in eastern coastal China and northeastern China.

The differences in surface air temperature in IRUN were found to be stronger EAWM-related cooling than those of the PRUN simulations over a large fraction of China (Figure 8b), but the differences in dust-induced RF at the surface are positive over most of China and heating the surface (Figure 6e). The EAWM difference (strongest minus weakest) over the Maritime Continent Low is enhanced in IRUN compared to PRUN (comparing Figure 8d to Figure 8c), partly due to the increased direct RF variations shown in Figure 6e. The combined result of the weaker Siberian High and the enhanced Maritime Continent Low in IRUN is that cold air is prevented from being transported from Siberia, Kazakhstan, western and central China to the western Pacific Ocean because of the anomalous northerlies over central China (Figures 8f and 8h). Therefore, the feedback of changes in surface winds on dust emissions enhances the differences in surface air temperatures between the strongest and weakest EAWM years, which result in decreased surface air temperatures of 0.6 K over central China and of up to 2 K over the Tibetan Plateau. Since the dust aerosols cool the surface air temperatures by 0.8 to 1.5 K over central China in winter [Sun and Liu, 2015; Zhao et al., 2015], the interannual variations in temperature show magnitudes similar to those of the wind-induced changes in dust emissions. Moreover, the magnitude of this cooling effect is significant when compared to that of modern anthropogenic aerosols. For example, Jiang et al. [2015] suggested that anthropogenic aerosols cool surface air temperatures by up to 1.2 K over eastern and central China, while heating the Tibetan Plateau by up to 1.8 K. While the anthropogenic aerosols are found to increase by up to 25% over southern China but decrease in the rest of China between the strongest and weakest EAWM years (strongest minus weakest [Jeong and Park, 2017]), it indicates that the interannual variations of anthropogenic aerosol strengthen the aerosol-induced cooling effect in southern China while weakening the cooling effect in other regions. Our results illustrate that the interannual variations in natural aerosols might offset the strength of the cooling effect over the southern part of coastal China (south of 30°N) that results from interannual variations of anthropogenic aerosols, while also weakening the cooling effect over the northern part of coastal China (north of 30°N). Over

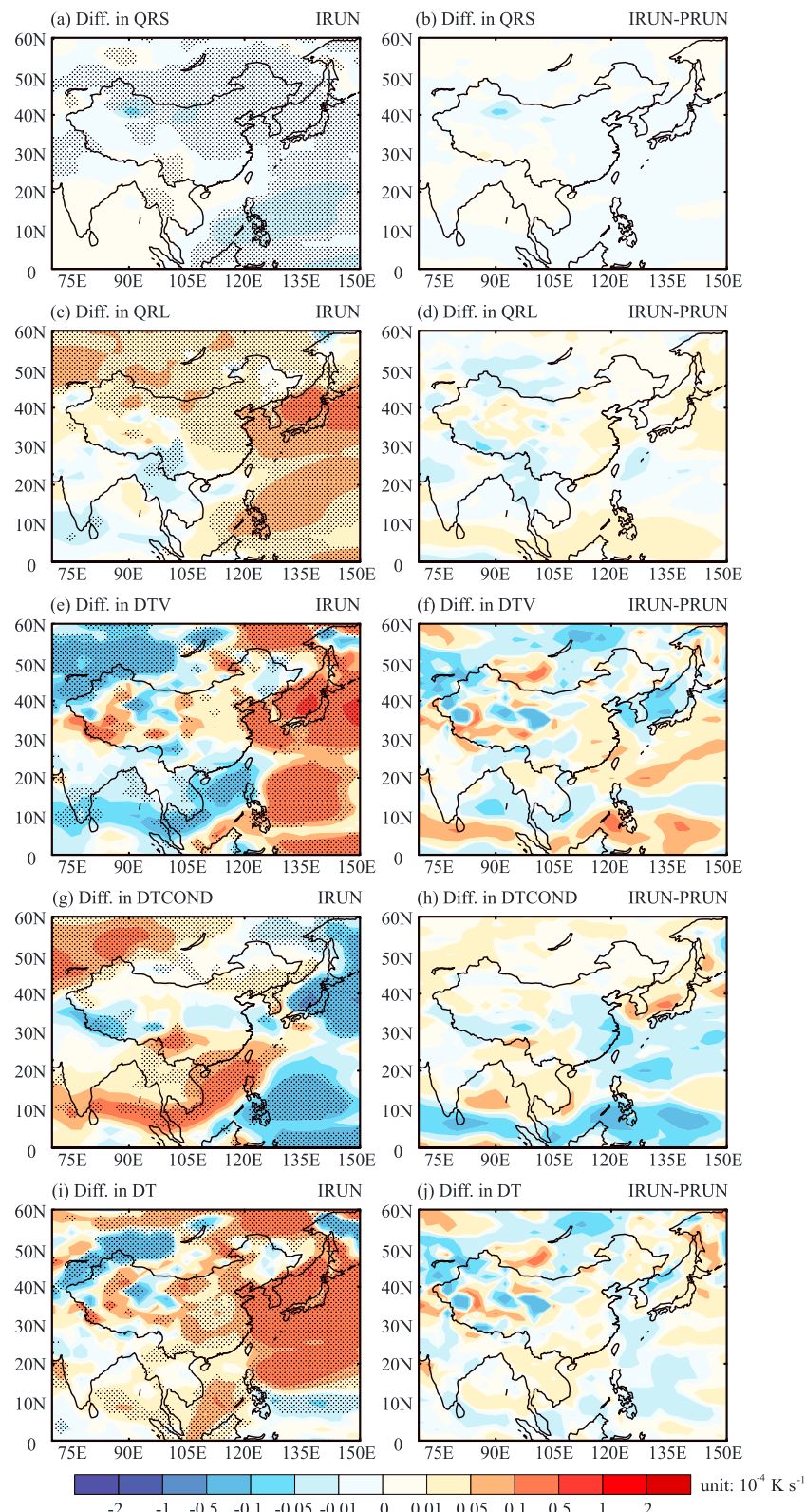


Figure 9. The differences between strongest and weakest EAWM years (strongest-weakest) from IRUN and the differences between IRUN and PRUN in surface-layer heating rate from (a and b) solar, (c and d) longwave, (e and f) temperature tendency with moist processes, (g and h) temperature vertical diffusion, and (i and j) total of above. The dotted areas indicate statistical significance with 95% (P value < 0.05) from a two-tailed Student's t test. The unit is 10^{-4} K s^{-1} .

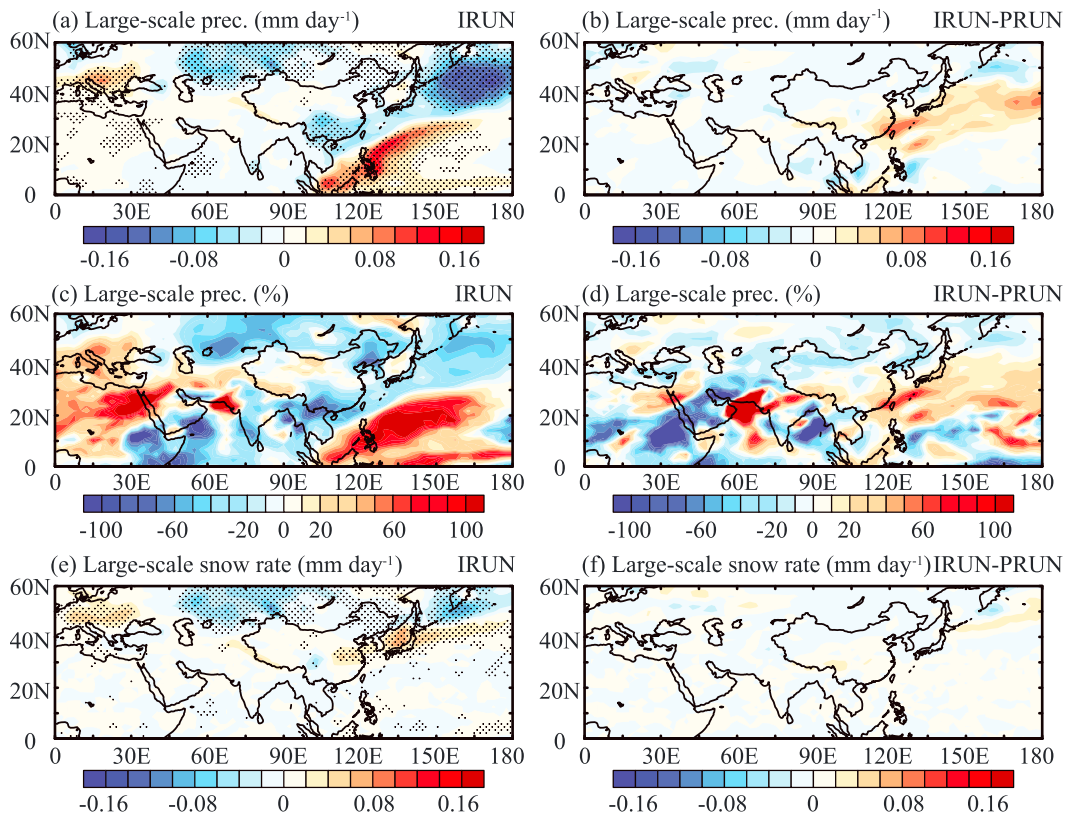


Figure 10. Horizontal distributions of (a and b) absolute and (c and d) percentage differences in large-scale precipitation (liquid + ice), and (e and f) differences in snow rate between strongest and weakest EAWM years (strongest-weakest). Figures 10a, 10c, and 10e show the differences calculated from IRUN simulation, while Figures 10b, 10d, and 10f compare the EAWM difference between IRUN and PRUN. The relative difference in Figures 10c and 10d calculated as $100\% \times \frac{\text{IRUN}_{\text{strong}} - \text{IRUN}_{\text{weak}}}{\text{IRUN}_{\text{mean}}}$ and $100\% \times \frac{(\text{IRUN}_{\text{strong}} - \text{IRUN}_{\text{weak}}) - (\text{PRUN}_{\text{strong}} - \text{PRUN}_{\text{weak}})}{\text{IRUN}_{\text{mean}}}$, respectively. The dotted areas indicate statistical significance with 95% (P value < 0.05) from a two-tailed Student's t test.

central China, the interannual variations of dust enhance the EAWM-related cooling, while the anthropogenic aerosols shrink the cooling.

The differences in large-scale precipitation (liquid and ice) in IRUN between the strongest and weakest EAWM years are shown in Figure 10. In the strongest EAWM years, reduced large-scale precipitation is simulated over the midlatitude continent from southern China to the northwestern Pacific Ocean, while increased precipitation is simulated over the Maritime Continent (Figure 10a), in agreement with previous studies that suggested that strong EAWM years have enhanced precipitation over low latitudes and suppressed precipitation at midlatitudes [Wang and Chen, 2010; Wang and Feng, 2011]. The simulated reduction of large-scale precipitation is $0.02\text{--}0.06 \text{ mm d}^{-1}$ (10–60% of the climatological mean preindustrial IRUN precipitation in winter) over southern China and less than 0.02 mm d^{-1} (10–50%) over northeastern China (Figures 10a and 10c). However, the snow rate is increased over midlatitudes from the middle reaches of the Yangtze River to Japan as a result of the cooling in those regions (Figures 8a and 10e). Comparing the differences in precipitation between IRUN and PRUN, the feedback of the EAWM-related changes in wind on dust emissions decreases variations of large-scale precipitation over eastern coastal China, with maximum values of 0.06 mm d^{-1} or 30% of the mean IRUN precipitation and show positive anomalies (Figures 10b and 10d). The differences in number concentration of cloud condensation nuclei (CCN) at 0.1% supersaturation ($\text{CCN}_{0.1}$) at 915 hPa and the cloud liquid water path (LWP) in IRUN were higher than those of the PRUN over eastern coastal China by 5–10% and 5–15 g m^{-2} , respectively (Figures 11b and 11d). The increase (decrease) in CCN should lead to a reduction (increase) of the precipitation efficiency with smaller (larger) cloud droplets. Therefore, an increase in variations of precipitation efficiency should be found because of the larger differences in EAWM-related CCN in IRUN than those in PRUN. However, the decrease in variations of

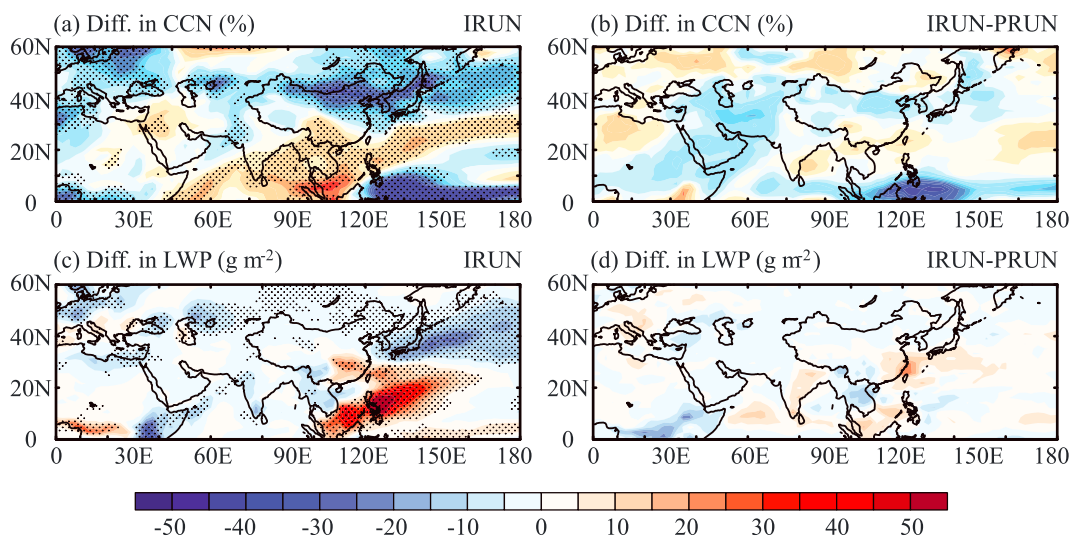


Figure 11. Horizontal distributions of (a and b) percentage differences in cloud condensation nucleus (CCN) number concentration at supersaturation of 0.1% ($\text{CCN}_{0.1}$) at 915 hPa, and the absolute differences in (c and d) the cloud liquid water path (LWP, unit: g m^{-2}) between strongest and weakest EAWM years (strongest-weakest). Figures 11a and 11c show the differences calculated from IRUN simulation, while Figures 11b and 11d compare the EAWM difference between IRUN and PRUN. The relative difference in Figures 11a and 11b calculated as $100\% \times \frac{\text{IRUN}_{\text{strong}} - \text{IRUN}_{\text{weak}}}{\text{IRUN}_{\text{mean}}}$ and $100\% \times \frac{(\text{IRUN}_{\text{strong}} - \text{IRUN}_{\text{weak}}) - (\text{PRUN}_{\text{strong}} - \text{PRUN}_{\text{weak}})}{\text{IRUN}_{\text{mean}}}$, respectively. The dotted areas indicate statistical significance with 95% (P value < 0.05) from a two-tailed Student's *t* test.

precipitation with increasing changes in CCN and LWP in eastern coastal of China indicates that the microphysical effects of dust aerosol do not play an important role in this region (Figures 10b and 11d). The decreasing changes in precipitation are the result of the reduced variations of northwesterlies over northeastern China and eastern coastal China in the lower troposphere which bring dry and cold air from Siberia to these regions (Figure 8f). The EAWM-related differences in large-scale precipitation are also weaker in central and northern China in IRUN than those in PRUN (Figure 10b). However, the differences in snow rate show a slight increase over central China (Figure 10f), consistent with the increasing changes in surface air temperature (Figure 8b). These results suggest that the feedback of the changes in surface winds on the interactive dust emissions weakens (strengthen) the dry and cold air across southeastern China in strongest (weakest) EAWM years, thereby increasing (decreasing) precipitation in these regions.

Note that the significant reduction in EAWM-related precipitation in the interactive simulation over southern and northeastern China (Figure 10a) should allow more dust by decreasing in the wet removal process. However, the fact that there is less dust in these regions indicates the reduction in emissions is larger than the reduction in wet removal.

4. Conclusions and Implications

We evaluate the magnitude of the feedback of the EAWM-related changes in wind on interactive dust emissions over East Asia in winter, including interannual variations of surface air temperature, sea level pressure, and precipitation using CESM. Since EAWM dominates the interannual variations in temperature in winter, an East Asian winter monsoon index (EAWMI) [Wang and Chen, 2014] is used to identify the EAWM-related variations. Using 150 year simulations, the climatological mean-simulated dust DOD in the interactive dust emission IRUN captures both the pattern and magnitude of large AODs retrieved from the Multi-angle Imaging SpectroRadiometer (MISR) during 2000–2012 over the Taklamakan and Gobi deserts. The simulated mean temperatures, sea level pressures (SLP), and wind fields at 850 hPa are consistent with NCEP reanalysis for 1948–2014.

Both simulated DJF dust concentrations and TOMS AI show lower (or higher) values in stronger (or weaker) EAWM years over northern China. The regional mean differences in dust column burden and DOD between

strongest and weakest EAWM years are 25% and 27.3% over the Taklamakan desert and 37.7% and 47.2% over the Gobi desert, respectively. The decreases in dust concentration lead to an increase in the net radiative forcing (RF) at the surface, with maximum values of 1.5 W m^{-2} over the Loess Plateau, the North China Plain, and the Gobi and Taklamakan deserts. The EAWM-related differences in interactive IRUN dust column burden and DOD decreased by up to 60 mg m^{-2} and 0.06 more compared to those in PRUN over the Taklamakan and Gobi deserts, and by up to 40 mg m^{-2} and 0.04 more over the downwind region. Therefore, the variations of net RF at the surface is increased by up to 1 W m^{-2} over the Loess Plateau, the North China Plain and the Taklamakan desert. The differences between the interactive and prescribed dust emission simulations show the effects of the feedback of EAWM-related changes in surface winds on dust emissions. Further, the wind-induced changes in dust emissions contribute about 67% to the variations in dust radiative forcing during winter and offset the cooling in the strongest EAWM years in eastern and northern China.

In the strongest EAWM years, the simulated surface air temperature cools by 1–3.5 K over eastern China compared to those in the weakest years. The feedback of the EAWM-related changes in surface winds on dust emissions decreases the variations of surface air temperature by up to 0.4 K from eastern coastal China to over the Sea of Japan (Figure 8b) and 0.6 K over northeastern China, resulting partly from the strong positive dust-induced radiation change at the surface, the weak variations of turbulent heat at the surface, and partly from the anomalous circulation that is caused by changes in the land-sea SLP differences. These results indicate that the interannual variations in dust emissions weaken the impact of EAWM on surface air temperature by 3–18% in eastern coastal China and northeastern China.

Over central and western China, the feedback of changes in surface winds on dust emissions enhances the differences in surface air temperature between the strongest and weakest EAWM years, which results in decreased surface air temperatures of 0.6 K over central China and of up to 2 K around the Tibetan Plateau. The cold air is prevented from being transported from Siberia, Kazakhstan, western and central China to the western Pacific Ocean because of the anomalous northerlies over central China due to the weaker Siberian High and the enhanced Maritime Continent Low in IRUN. Comparing the differences in precipitation between IRUN and PRUN, the feedback of the EAWM-related changes in wind on dust emissions also decreases the large-scale precipitation variations over eastern coastal China by 10–30% because of the reduced changes in northwesterly which bring dry and cold air from Siberia to these regions. Considering the increase (decrease) in CCN and LWP in this region during the strongest (weakest) EAWM years, the microphysical effect of dust aerosol does not contribute to the decrease (increase) in precipitation over eastern coastal China. The weaker cooling over eastern coastal China due to the feedback of changes in wind on dust emissions could offset the stronger cooling and drying caused by the interannual variations of anthropogenic aerosols over the southern part of East Asia (south of 30°N) in the strongest EAWM years than those in weakest EAWM years by up to 67%, while weakening the cooling over the northern part of East Asia (north of 30°N) when the interannual variations of anthropogenic aerosols also do so with similar contributions. Moreover, the anomalous circulation would further impact the anthropogenic aerosol concentration and distribution [Yang et al., 2017].

The major results of this study do not change if the other EAWM index is applied. For example, with a EAWMI calculated based on wind [Lou et al., 2016], although the interannual variations in SLP are not as significant as those in this study (Figure S6), the EAWM-related dust concentration also decreases over dust source regions (Figure S7a) and increases the direct shortwave radiative forcing (SWRF) over the North China Plain, the Gobi desert, and the Taklamakan desert but with smaller variations than this study. Relative to the PRUN, the variations of SWRF between the strongest and weakest EAWM years are larger in IRUN over the North China Plain, indicating that the wind-induced changes in dust emissions heat the surface and offset the cooling. The simulated differences in surface air temperature and wind fields at 850 hPa between the strongest and weakest EAWM years are shown in Figures S8a and S8c, respectively, consistent with the spatial distribution shown in Figures 8a and 8e, but with smaller variations over eastern China. Compared to PRUN, the EAWM-related surface air temperature also shows negative changes over central China in PRUN but positive over eastern coastal China (Figure S8b), in agreement with Figure 8b. These results also show that the feedback of the EAWM-related changes in surface winds on dust emissions weaken the impact of EAWM on surface temperature. Since the strongest and weakest years are different from those found with the other index, the variations in dust emissions weaken the EAWM-related surface air temperature by up to 40%

over east coastal and northeastern China. However, the EAWM-related large-scale precipitation is found to be more sensitive to the EAWM in comparing Figure S8e to Figure 10a. Therefore, the feedback of the EAWM-related changes in wind on dust emissions shows a different pattern because of the variations in the dynamic cycle (Figures 10b and S8f).

Wind-induced differences in sea-salt aerosol between the strongest and weakest EAWM years also impact the radiative forcing over the northern Pacific Ocean and the Maritime Continent through both direct and indirect climate effects [Ma *et al.*, 2008; Yang *et al.*, 2016a]. For example, the variation in sea-salt aerosol increased over the Maritime Continent because of the anomalous circulation resulting from the differences between the interactive and prescribed dust emission simulations. The difference between the strongest and weakest EAWM years in direct RF due to aerosol in IRUN compared to PRUN increased at the surface over the Maritime Continent, with a maximum value of 0.75 W m^{-2} (Figure 6e). The increase in RF caused heating of sea surface temperatures and enhancement of the Maritime Continent Low. The weaker Maritime Continent Low with its impacts on sea salt and RF leads to a strong anomalous circulation, which brings warm air from the ocean to the continent. As a result, the variations in temperature would be smaller if interannual variations of only dust emissions were separately taken into account. Moreover, a recent study suggested that the dust in the atmosphere is substantially coarser than represented in the CESM model [Kok *et al.*, 2017], which implies a larger negative radiative forcing of dust if the lifetime changes are not taken into account. Based on the interactive IRUN simulation in this study, the global mean radiative forcing at TOA is -1.15 W m^{-2} , obviously beyond the range of -0.48 to $+0.2 \text{ W m}^{-2}$ reported by Kok *et al.* [2017]. Meanwhile, the dust absorption simulated by CESM is higher than observed in modern records [Di Biagio *et al.*, 2014; Denjean *et al.*, 2016]. Since our model underestimates the dust size and overestimates the dust absorption, the direct radiative forcing induced by dust aerosol over eastern China simulated at the surface is also biased high.

Previous studies suggested that the precipitation reduces dust emissions mainly through suppressing emissions when snow covers the potential dust source areas and increasing soil moisture when snow melts [Tanaka *et al.*, 2011; Lee and Kim, 2012]. Therefore, the slight increase in snow rate over Taklamakan and Gobi deserts in the strongest EAWM years than those in the weakest EAWM years (Figure 10e) further reduces the dust emissions in the interactive simulation. The effects of the feedback of EAWM-related changes in surface wind on dust emissions decreases (increases) the large-scale snow rate around dust source regions during the strongest (weakest) EAWM years (Figure 10f), which enhance the interannual variations of dust concentrations. Further, the feedback of the EAWM-related changes in wind on dust emissions leads to an increase (decrease) in precipitation over eastern coastal China in the strongest (weakest) EAWM years, a decrease (increase) in the dust concentrations through the wet removal process, and enhanced changes in dust radiative forcing.

Acknowledgments

This research was supported by National Science Foundation AGS1048995 and by DOE DE-SC0006679 as part of the U.S. Department of Energy, Office of Science, Biological and Environmental Research, Decadal and Regional Climate Prediction using Earth System Models (EaSM) program. The Pacific Northwest National Laboratory is operated for the DOE by Battelle Memorial Institute under contract DE-AC05-76RLO 1830. NCEP Reanalysis data sets are provided by the NOAA/OAR/ESRL PSD, Boulder, Colorado, USA, from their Web site at <http://www.esrl.noaa.gov/psd/>. The satellite-derived Total Ozone Mapping Spectrometer Aerosol Index (TOMS AI) monthly data sets are obtained from the Web site at <http://www.ouce.ox.ac.uk/~clivar/tomsai/aiinput.html>. Multi-angle Imaging SpectroRadiometer (MISR) data sets are provided by NASA's Jet Propulsion Laboratory, Pasadena, California, from their Web site at <https://eosweb.larc.nasa.gov/project/misr/>. We acknowledge the AERONET principal PI for their effort in establishing and maintaining the AERONET sites used in this research. This research used resources of the National Energy Research Scientific Computing Center (NERSC) under contract DE-AC02-05CH11231. The data and codes for these results are posted at http://portal.nersc.gov/project/m1374/EAM_DUST.

References

- Carlson, T. N., and S. G. Benjamin (1980), Radiative heating rates for Saharan dust, *J. Atmos. Sci.*, 37, 193–213, doi:10.1175/1520-0469(1980)037<0193:RHRSD>2.0.CO;2.
- Chen, W., D. W. Fryrear, and Z. Yang (1999), Dust fall in the Taklamakan desert of China, *Phys. Geogr.*, 20, 189–224.
- Chen, S., et al. (2014), Regional modeling of dust mass balance and radiative forcing over East Asia using WRF-Chem, *Aeolian Res.*, 15, 15–30, doi:10.1016/j.aeolia.2014.02.001.
- Denjean, C., et al. (2016), Size distribution and optical properties of mineral dust aerosols transported in the western Mediterranean, *Atmos. Chem. Phys.*, 16, 1081–1104, doi:10.5194/acp-16-1081-2016.
- Di Biagio, C. D., H. Boucher, S. Caquineau, S. Chevaillier, J. Cuesta, and P. Formenti (2014), Variability of the infrared complex refractive index of African mineral dust: Experimental estimation and implications for radiative transfer and satellite remote sensing, *Atmos. Chem. Phys.*, 14, 11,093–11,116, doi:10.5194/acp-14-11093-2014.
- Ghan, S. J. (2013), Technical note: Estimating aerosol effects on cloud radiative forcing, *Atmos. Chem. Phys.*, 13, 9971–9974, doi:10.5194/acp-13-9971-2013.
- Ghan, S. J., and R. A. Zaveri (2007), Parameterization of optical properties for hydrated internally mixed aerosol, *J. Geophys. Res.*, 112, D10201, doi:10.1029/2006JD007927.
- Ginoux, P. J., M. Prospero, T. E. Gill, N. Christina Hsu, and M. Zhao (2012), Global-scale attribution of anthropogenic and natural dust sources and their emission rates based on MODIS Deep Blue aerosol products, *Rev. Geophys.*, 50, RG3005, doi:10.1029/2012RG000388.
- Gu, Y., K. N. Liou, W. Chen, and H. Liao (2010), Direct climate effect of black carbon in China and its impact on dust storms, *J. Geophys. Res.*, 115, D00K14, doi:10.1029/2009JD013427.
- Gu, Y., Y. Xue, F. De Sales, and K. N. Liou (2016), A GCM investigation of dust aerosol impact on the regional climate of North Africa and South/East Asia, *Clim. Dyn.*, 46, 2353, doi:10.1007/s00382-015-2706-y.
- Hao, Z., D. Sun, and J. Zheng (2015), East Asian Monsoon signals reflected in temperature and precipitation changes over the past 300 years in the middle and lower reaches of the Yangtze River, *PLoS One*, 10(6), e0131159, doi:10.1371/journal.pone.0131159.

- Helmhert, J., B. Heinold, I. Tegen, O. Hellmuth, and M. Wendisch (2007), On the direct and semi-direct effect of Saharan dust over Europe: A modeling study, *J. Geophys. Res.*, 112, D13208, doi:10.1029/2006JD007444.
- Hess, M., P. Koepke, and I. Schult (1998), Optical properties of aerosols and clouds: The software package OPAC, *Bull. Am. Meteorol. Soc.*, 79(5), 831–844.
- Hurrell, J. W., et al. (2013), The Community Earth System Model: A framework for collaborative research, *Bull. Am. Meteorol. Soc.*, 94, 1339–1360, doi:10.1175/BAMS-D-12-00121.1.
- IPCC (2013), Climate change 2013: The physical science basis, in *Contribution of Working Group I to the Fifth Assessment Report of the Intergovernmental Panel on Climate Change*, edited by T. F. Stocker et al., pp. 1–1535, Cambridge Univ. Press, Cambridge, U. K., and New York.
- Jeong, J. I., and R. J. Park (2017), Winter monsoon variability and its impact on aerosol concentrations in East Asia, *Environ. Pollut.*, 221, 285–292, doi:10.1016/j.envpol.2016.11.075.
- Jiang, Y., X. Yang, and X. Liu (2015), Seasonality in anthropogenic aerosol effects on East Asian climate simulated with CAM5, *J. Geophys. Res. Atmos.*, 120, 10,837–10,861, doi:10.1002/2015JD023451.
- Ju, L., and Z. Han (2011), Direct radiative forcing and climatic effects of aerosols over East Asia by RegCM3, *Atmos. Oceanic Sci. Lett.*, 4, 363–367, doi:10.1080/16742834.2011.11446954.
- Jugder, D., M. Shinoda, N. Sugimoto, I. Matsui, M. Nishikawa, S.-U. Park, Y.-S. Chun, and M.-S. Park (2011), Spatial and temporal variations of dust concentrations in the Gobi Desert of Mongolia, *Global Planet. Change*, 78, 14–22, doi:10.1016/j.gloplacha.2011.05.003.
- Kanai, Y., et al. (2005), Characterization of Aeolian dust in East China and Japan from 2001 to 2003, *J. Meteorol. Soc. Jpn.*, 83A, 73–106.
- Kim, Y., K.-Y. Kim, and J.-G. Jhun (2013), Seasonal evolution mechanism of the East Asian winter monsoon and its interannual variability, *Clim. Dyn.*, 41, 1213–1228, doi:10.1007/s00382-012-1491-0.
- Kok, J. F., D. A. Ridley, Q. Zhou, R. L. Miller, C. Zhao, C. L. Heald, D. S. Ward, S. Albani, and K. Haustein (2017), Smaller desert dust cooling effect estimated from analysis of dust size and abundance, *Nat. Geosci.*, 10, 274–278, doi:10.1038/NGEO2912.
- Lee, J.-J., and C.-H. Kim (2012), Roles of surface wind, NDVI and snow cover in the recent changes in Asian dust storm storm occurrence frequency, *Atmos. Environ.*, 59, 366–375, doi:10.1016/j.atmosenv.2012.05.022.
- Li, X., and H. Zhang (2012), Seasonal variations in dust concentration and dust emission observed over Horqin Sandy Land area in China from December 2010 to November 2011, *Atmos. Environ.*, 61, 56–65, doi:10.1016/j.atmosenv.2012.07.007.
- Li, Z., K. Lee, Y. Wang, J. Xin, and W. Hao (2010), First observation-based estimates of cloud-free aerosol radiative forcing across China, *J. Geophys. Res.*, 115, D00K18, doi:10.1029/2009JD013306.
- Li, Z., et al. (2016), Aerosol and monsoon climate interactions over Asia, *Rev. Geophys.*, 54, 866–929, doi:10.1002/2015RG000500.
- Liao, H., and J. H. Seinfeld (1998), Radiative forcing by mineral dust aerosols: Sensitivity to key variables, *J. Geophys. Res.*, 103, 31,637–31,645, doi:10.1029/1998JD200036.
- Liu, X., et al. (2012), Toward a minimal representation of aerosols in climate models: Description and evaluation in the Community Atmosphere Model CAM5, *Geosci. Model Dev.*, 5, 709–739, doi:10.5194/gmd-5-709-2012.
- Lou, S., L. Russell, Y. Yang, L. Xu, M. A. Lamjiri, M. J. DeFlorio, A. J. Miller, S. J. Ghan, Y. Liu, and B. Singh (2016), Impacts of the East Asian Monsoon on springtime dust concentrations over China, *J. Geophys. Res. Atmos.*, 121, 8137–8152, doi:10.1002/2016JD024758.
- Ma, X., K. von Salzen, and J. Li (2008), Modelling sea salt aerosol and its direct and indirect effects on climate, *Atmos. Chem. Phys.*, 8, 1311–1327, doi:10.5194/acp-8-1311-2008.
- Mahowald, N., D. R. Muhs, S. Levis, P. J. Rasch, M. Yoshioka, C. S. Zender, and C. Luo (2006a), Change in atmospheric mineral aerosols in response to climate: Last glacial period, preindustrial, modern, and doubled carbon dioxide climates, *J. Geophys. Res.*, 111, D10202, doi:10.1029/2005JD006653.
- Mahowald, N., M. Yoshioka, W. Collins, A. Conley, D. Fillmore, and D. Coleman (2006b), Climate response and radiative forcing from mineral aerosols during the last glacial maximum, pre-industrial and doubled-carbon dioxide climates, *Geophys. Res. Lett.*, 33, L20705, doi:10.1029/2006GL026126.
- Merrill, J. T., M. Uematsu, and R. Bleck (1989), Meteorological analysis of long range transport of mineral aerosols over the North Pacific, *J. Geophys. Res.*, 94, 8584–8598, doi:10.1029/JD094iD06p08584.
- Miller, R. L., and I. Tegen (1998), Climate response to soil dust aerosols, *J. Clim.*, 11(12), 3247–3267, doi:10.1175/1520-0442(1998)011<3247:CRRTSDA>2.0.CO;2.
- Miller, R. L., J. Perlitz, and I. Tegen (2004), Modeling Arabian dust mobilization during the Asian summer monsoon: The effect of prescribed versus calculated SST, *Geophys. Res. Lett.*, 31, L22214, doi:10.1029/2004GL020669.
- Priyith, S. S., M. Aloysius, and M. Mohan (2013), Global aerosol source/sink map, *Atmos. Environ.*, 80, 533–539, doi:10.1016/j.atmosenv.2013.08.038.
- Sassen, K. (2002), Indirect climate forcing over the western US from Asian dust storms, *Geophys. Res. Lett.*, 29(10), 1465, doi:10.1029/2001GL014051.
- Shioya, M., R. Kawamura, H. Hatushika, and S. Iizuka (2011), Influence of the East Asian winter monsoon variability on the surface cyclogenesis over the East China Sea in late winter, *SOLA*, 7, 129–132, doi:10.2151/sola.2011-033.
- Smith, R., et al. (2010), The Parallel Ocean Program (POP) reference manual. Tech. Rep. LAUR-10-01853, Los Alamos Natl. Lab.
- Sokolik, I. N., and O. B. Toon (1996), Direct radiative forcing by anthropogenic airborne mineral aerosols, *Nature*, 381, 681–683, doi:10.1038/381681a0.
- Sokolik, I. N., D. M. Winker, G. Bergametti, D. A. Gillette, G. Carmichael, Y. J. Kaufman, L. Gomes, L. Schuetz, and J. E. Penner (2001), Introduction to special section: Outstanding problems in quantifying the radiative impacts of mineral dust, *J. Geophys. Res.*, 106, 18,015–18,027, doi:10.1029/2000JD900498.
- Sun, H., and X. Liu (2015), Numerical simulation of the direct radiative effects of dust aerosols on the East Asian Winter monsoon, *Adv. Meteorol.*, 142617, doi:10.1155/2015/142617.
- Sun, J., M. Zhang, and T. Liu (2001), Spatial and temporal characteristics of dust storms in China and its surrounding regions, 1960–1999: Relations to source area and climate, *J. Geophys. Res.*, 106, 10,325–10,333, doi:10.1029/2000JD900665.
- Sun, H., Z. Pan, and X. Liu (2012), Numerical simulation of spatial-temporal distribution of dust aerosol and its direct radiative effects on East Asian climate, *J. Geophys. Res.*, 117, D13206, doi:10.1029/2011JD017219.
- Tanaka, T. Y., T. T. Sekiyama, T. Maki, and M. Mikami (2011), The effects of snow cover and soil moisture on Asian dust: I. A numerical sensitivity study, *SOLA*, 7A, 36–39, doi:10.2151/sola.7A-010.
- Tegen, I., S. P. Harrison, K. Kohfeld, I. C. Prentice, M. Coe, and M. Heimann, 2002: Impact of vegetation and preferential source areas on global dust aerosol: Results from a model study. *J. Geophys. Res.*, 107(D21), 4576, doi:10.1029/2001JD000963.

- Wang, L., and W. Chen (2010), How well do existing indices measure the strength of the East Asian winter monsoon?, *Adv. Atmos. Sci.*, 27, 855–870, doi:10.1007/s00376-009-9094-3.
- Wang, L., and W. Chen (2014), An intensity index for the East Asian winter monsoon, *J. Clim.*, 27, 2361–2374, doi:10.1175/JCLI-D-13-00086.1.
- Wang, L., and J. Feng (2011), Two major modes of the wintertime precipitation over China, *Chin. J. Atmos. Sci.*, 35, 1105–1116.
- Wang, Y. Q., X. Y. Zhang, J. Y. Sun, X. C. Zhang, H. Z. Che, and Y. Li (2015), Spatial and temporal variations of the concentrations of PM10, PM2.5 and PM1 in China, *Atmos. Chem. Phys.*, 15, 13,585–13,598, doi:10.5194/acp-15-13585-2015.
- Wu, Y., R. Zhang, Z. Han, and Z. Zeng (2010), Relationship between East Asian Monsoon and dust weather frequency over Beijing, *Adv. Atmos.*, 27, 1389–1398, doi:10.1007/s00376-010-9181-5.
- Xi, X., and I. N. Sokolik (2012), Impact of Asian dust aerosol and surface albedo on photosynthetically active radiation and surface radiative balance in dryland ecosystems, *Adv. Meteorol.*, 276207, doi:10.1155/2012/276207.
- Xi, X., and I. N. Sokolik (2015), Seasonal dynamics of threshold friction velocity and dust emission in Central Asia, *J. Geophys. Res. Atmos.*, 120, 1536–1564, doi:10.1002/2014JD022471.
- Xin, J., C. Gong, S. Wang, and Y. Wang (2016), Aerosol direct radiative forcing in desert and semi-desert regions of northwestern China, *Atmos. Res.*, 171, 56–65, doi:10.1016/j.atmosres.2015.12.004.
- Xuan, J., and I. N. Sokolik (2002), Characterization of sources and emission rates of mineral dust in Northern China, *Atmos. Environ.*, 36, 4863–4876, doi:10.1016/S1352-2310(02)00585-X.
- Yang, Y., H. Liao, and J. Li (2014), Impacts of the East Asian summer monsoon on interannual variations of summertime surface-layer ozone concentrations over China, *Atmos. Chem. Phys.*, 14, 6867–6879, doi:10.5194/acp-14-6867-2014.
- Yang, Y., et al. (2016a), Impacts of ENSO events on cloud radiative effects in preindustrial conditions: Changes in cloud fraction and their dependence on interactive aerosol emissions and concentrations, *J. Geophys. Res. Atmos.*, 121, 6321–6335, doi:10.1002/2015JD024503.
- Yang, Y., L. M. Russell, S. Lou, Y. Liu, B. Singh, and S. J. Ghan (2016b), Rain-aerosol relationships influenced by wind speed, *Geophys. Res. Lett.*, 43, 2267–2274, doi:10.1002/2016GL067770.
- Yang, Y., L. Russell, S. Lou, M. A. Lamjiri, Y. Liu, B. Singh, and S. Ghan (2016c), Changes in sea salt emissions enhance ENSO variability, *J. Clim.*, 29, 8575–8588, doi:10.1175/JCLI-D-16-0237.1.
- Yang, Y., L. M. Russell, S. Lou, H. Liao, J. Guo, Y. Liu, B. Singh, and S. J. Ghan (2017), Dust-wind interactions can intensify aerosol pollution over eastern China, *Nat. Commun.*, 8, 15333, doi:10.1038/ncomms15333.
- Yue, X., H. Liao, H. J. Wang, S. L. Li, and J. P. Tang (2011), Role of sea surface temperature responses in simulation of the climatic effect of mineral dust aerosol, *Atmos. Chem. Phys.*, 11, 6049–6062, doi:10.5194/acp-11-6049-2011.
- Zender, C. S., H. Bian, and D. L. Newman, 2003: The mineral dust entrainment and deposition (DEAD) model: description and 1990s dust climatology. *J. Geophys. Res.*, 108(D14), 4416, doi:10.1029/2002JD002775.
- Zhang, X., Z. Shen, G. Zhang, T. Chen, and H. Liu (1996), Remote mineral aerosol in westerlies and their contributions to Chinese loess, *Sci. China, Ser. D*, 39, 67–76.
- Zhang, X., R. Arimoto, and Z. S. An (1997), Dust emission from Chinese desert sources linked to variations in atmospheric circulation, *J. Geophys. Res.*, 102, 28,041–28,047, doi:10.1029/97JD02300.
- Zhang, X., R. Arimoto, G. H. Zhu, T. Chen, and G. Y. Zhang (1998), Concentration, size-distribution and deposition of mineral aerosol over Chinese desert regions, *Tellus B*, 50, 317–330, doi:10.1034/j.1600-0889.1998.t01-3-0001.x.
- Zhang, X., S. L. Gong, T. L. Zhao, R. Arimoto, Y. Q. Wang, and Z. J. Zhou (2003), Sources of Asian dust and role of climate change evrsus desertification in Asian dust emission, *Geophys. Res. Lett.*, 30(30), 2272, doi:10.1029/2003GL018206.
- Zhang, X. Y., Y. Q. Wang, T. Niu, X. C. Zhang, S. L. Gong, Y. M. Zhang, and J. Y. Sun (2012), Atmospheric aerosol compositions in China: Spatial/temporal variability, chemical signature, regional haze distribution and comparisons with global aerosols, *Atmos. Chem. Phys.*, 12, 779–799, doi:10.5194/acp-12-779-2012.
- Zhao, T. L., S. L. Gong, X. Y. Zhang, J.-P. Blanchet, I. G. McKendry, and Z. J. Zhou (2006), A simulated climatology of Asian dust aerosol and its trans-pacific transport. Part I: Mean climate and validation, *J. Clim.*, 19, 88–103, doi:10.1175/JCLI3605.1.
- Zhao, S., H. Zhang, S. Feng, and Q. Fu (2015), Simulating direct effects of dust aerosol on arid and semi-arid regions using an aerosol-climate coupled system, *Int. J. Climatol.*, 35, 1858–1866, doi:10.1002/joc.4093.
- Zhou, L. T. (2011), Impact of East Asian winter monsoon on rainfall over southeastern China and its dynamical process, *Int. J. Climatol.*, 31, 677–686, doi:10.1002/joc.2101.